PCCP

Electrochemical phase transformation accompanied with Mg extraction and insertion in spinel $MgMn_2O_4$ cathode material

Journal:	*Physical Chemistry Chemical Physics*
Manuscript ID	CP-ART-08-2019-004461.R1
Article Type:	Paper
Date Submitted by the Author:	23-Sep-2019

Complete List of Authors:	Hatakeyama, Takuya; Tohoku University Institute for Materials Research, Okamoto, Norihiko; Tohoku University Institute for Materials Research Shimokawa, Kohei; Institute for Materials Research, Tohoku University, Li, Hongyi; Tohoku University, Institute for Materials Research Nakao, Aiko; Riken, Uchimoto, Yoshiharu; Kyoto University, Department of Energy & Hydrocarbon Chemistry, Graduate School of Engineering Tanimura, Hiroshi; Tohoku University Institute for Materials Research Kawaguchi, Tomoya; Tohoku University Institute for Materials Research Ichitsubo, Tetsu; Tohoku Daigaku, Institute for Materials Research

ARTICLE

Electrochemical phase transformation accompanied with Mg extraction and insertion in spinel $MgMn_2O_4$ cathode material

Received 00th January 20xx,
Accepted 00th January 20xx

DOI: 10.1039/x0xx00000x

Takuya Hatakeyama[a*], Norihiko L. Okamoto[a], Kohei Shimokawa[a], Hongyi Li[a], Aiko Nakao[b], Yoshiharu Uchimoto[c], Hiroshi Tanimura[a], Tomoya Kawaguchi[a] and Tetsu Ichitsubo[a*]

One of the key challenges in magnesium rechargeable battery (MRB) is to develop Mg-intercalation cathodes exhibiting higher redox potentials with larger specific capacities. Although the Mg-transition-metal spinel oxides have been shown to be an excellent candidate for the MRB cathode materials by utilizing the valence change from trivalent to divalent of transition metal with starting from Mg insertion, there is no clear evidence to date that Mg can be indeed extracted from the initial spinel hosts by utilizing the change from trivalent to quadrivalent. In this work, we clearly present various experimental evidences of electrochemical extraction of Mg from spinel $MgMn_2O_4$. The present electrochemical charge, i.e., extraction treatment of Mg, was performed in an ionic liquid at 150 °C to ensure Mg hopping in the spinel host. Our analyses show that Mg can be extracted from $Mg_{(1-x)}Mn_2O_4$ up to x = 0.4 and, afterwards, successively be inserted into the Mg-extracted (demagnesiated) host via two-phase reaction between tetragonal and cubic spinels. Finally, we also discuss the difference in electrochemical features between $LiMn_2O_4$ and $MgMn_2O_4$.

Introduction

Enhancing energy density of rechargeable batteries is one of major challenges for energy-storage science and technology[1,2]. Li-ion battery is a well-established system and currently dominant in portable electronic devices. On the other hand, emerging large-scale applications, such as electric vehicles and smart grids, demand more cost-effective batteries with high energy density[3-5]. One of viable alternatives to the Li-ion battery is a magnesium rechargeable battery (MRB) that employs magnesium metal as an anode. Notably, magnesium metal provides potentially higher volumetric capacity (3833 mAh/cm^3), exceeding lithium-intercalated graphite (746 mAh/cm^3) and even lithium metal (2050 mAh/cm^3). In addition, the global abundance of magnesium is beneficial for large-scale applications.

The development of magnesium rechargeable batteries is plagued by the absence of appropriate cathode materials, which is mainly due to sluggish Mg migration in common cathode materials[6,7]. In 2000, Aurbach *et al.* successfully demonstrated the first prototype of magnesium rechargeable battery employing Mo_6S_8 Chevrel phase as a cathode[8]. Although the Chevrel phase exhibits relatively fast Mg intercalation kinetics, the electrode potential of the Chevrel phase is unfortunately as low as 1.0-1.3 V vs. Mg^{2+}/Mg, resulting in poor energy density. Then, extensive studies have been carried out to develop higher potential cathodes, including $MgFeSiO_4$[9], V_2O_5[10], hollandite MnO_2[11], birnessite MnO_2[12-14], and spinel $MgCo_2O_4$[15,16].

Manganese spinel oxide λ-Mn_2O_4 is a well-known Li intercalation material that exhibits high potential of 3.8 V vs. Li^+/Li with keeping high stability against Li extraction[17-19]. By analogy with Li intercalation, a prime candidate for high potential Mg-intercalation cathode appears to be spinel $MgMn_2O_4$. According to the pioneering work of Kim *et al.*[20], it is reported that spinel-type delithiated (Li)Mn_2O_4 can allow Mg insertion in aqueous electrolytes with moderate kinetics even at ambient temperature, but in nonaqueous electrolytes, the Mg intercalation into spinel λ-Mn_2O_4 undergoes severe kinetic retardation. Around the same time, Okamoto and Ichitsubo *et al.* demonstrated that, by heating a nonaqueous electrolyte up to 150 °C, spinel compounds (e.g., $MgCo_2O_4$, Co_3O_4, $MgMn_2O_4$, etc) can accommodate Mg by undergoing spinel-to-rocksalt transition [16,21,22] with the valence change of transition metal from trivalent to divalent, being very similar to the 8*a*–16*c* transition in the $LiMn_2O_4$ system[23]. Furthermore, they also suggested that Mg can be extracted especially from $MgMn_2O_4$ or $MgCr_2O_4$ via valence change of Mn or Cr from trivalent to tetravalent[16]. However, there is no clear evidence for Mg deintercalation from the spinels in terms of composition, crystal structure change, and the reaction mechanism.

$MgMn_2O_4$ belongs to tetragonal space group ($I4_1/amd$) resulting from Jahn-Teller distortion of Mn(III) as well as tetragonal $Li_2Mn_2O_4$. In the case of $Li_2Mn_2O_4$ system, oxidation of Mn(III) by deintercalation of Li proceeds with two-phase

[a] *Institute for Materials Research, Tohoku University, Sendai 980-8577, Japan. E-mail: hatakeyama-t@imr.tohoku.ac.jp; tichi@imr.tohoku.ac.jp*
[b] *The Institute of Physical and Chemical Research (RIKEN), Saitama, 351-01, Japan*
[c] *Graduate School of Human and Environmental Studies, Kyoto University, Kyoto 606-8501, Japan*

Electronic Supplementary Information (ESI) available: Setup for electrochemical measurements, crystal structure of $MgMn_2O_4$, TEM image, XRD patterns upon Mg intercalation into spinel $MgMn_2O_4$, XPS spectra, simulation of XRD patterns. See DOI: 10.1039/x0xx00000x

reaction between tetragonal $Li_2Mn_2O_4$ and cubic $LiMn_2O_4$. The deintercalation of divalent Mg from $MgMn_2O_4$ would possibly cause some difference in the phase-transition mode. Here we focus on the spinel-type $MgMn_2O_4$ whose Mn valence can be utilized from tetravalent to divalent (by which it "theoretically" provides a large capacity of about 540 mAh/g) and report the feasibility of electrochemical Mg deintercalation from spinel $MgMn_2O_4$. Since, to our empirical knowledge, it is especially laborious to extract Mg from spinel oxides at ambient temperature, in the present work the $MgMn_2O_4$ electrodes were electrochemically oxidized at 150 °C in Cs/Mg-mixed ionic liquid, and subsequently they were characterized by the ICP elemental analysis and STEM/X-ray structural analysis. Our experimental study demonstrates, that Mg can be firmly deintercalated from $MgMn_2O_4$ at 150 °C and the deintercalation occurs through a two-phase transformation. This work sheds light on the high potential of spinel $MgMn_2O_4$ as a cathode material for magnesium rechargeable batteries with high energy density.

Experimental section

Synthesis

The powder of $MgMn_2O_4$ was synthesized through the Pechini's process. The starting materials of $Mg(NO_3)_2{\cdot}6H_2O$ (Nacalai Tesque, 99%), $Mn(NO_3)_2{\cdot}6H_2O$ (Nacalai Tesque, 98%) propylene glycol $C_3H_8O_2$ (Wako Pure Chemical, 99%), and citric acid $C_6H_8O_7$(Wako Pure Chemical, 98%) were weighed out in the molar ratio of 1.0: 2.0: 15: 60. After dissolution into propylene glycol, the solution was heated up to 200 °C to promote polymerization followed by baking at 300 °C to remove the excess of propylene glycol. The resulting powder was ball-milled in ethanol and then calcined for 10 hours in air at 425 °C.

Electrochemical measurement

Electrochemical measurements were performed in an Ar-filled glovebox using a three-electrode beaker cell shown in Fig. S1. To fabricate the working electrode, 80 wt% $MgMn_2O_4$, 10 wt% carbon black and 10 wt% polyvinylidene difluoride (PVDF) were first dispersed in N-methylpyrrolidone (NMP) solution. The resulting slurry was coated on aluminum foil and then dried at 120 °C in vacuum. The loading of $MgMn_2O_4$ on the electrode was 2.1 mg/cm^2. The beaker was filled with 6.0 g of electrolyte composed of 90 mol% CsTFSA (TFSA: bis(trifluoromethanesulfonyl)amide) and 10 mol% $Mg(TFSA)_2$. The electrolyte temperature was maintained at 150 °C during measurement. Mg metal ribbon was used as a counter electrode, and Li ribbon was used as a reference electrode, which was separated from the $CsTFSA/Mg(TFSA)_2$ electrolyte using a glass tube with a porous ceramic filter and immersed in N,N-diethyl-N-methyl-N-(2-methoxyethyl) ammonium bis(trifluoromethanesulfonyl)amide (DEMETFSA) dissolving 0.1 M LiTFSA; hereafter we refer this to as "LiRE". According to our previous experiment[16], the difference in the electrode potential between LiRE and Mg^{2+}/Mg is about 0.5 V. It is also shown that $CsTFSA/Mg(TFSA)_2$ electrolyte is tolerant to oxidative decomposition up to ~4.5 V vs. LiRE on a Pt electrode[16]. Cyclic voltammetry was conducted at a scan rate of 0.1 mV/s. Galvanostatic charge/discharge test was performed at a rate of 0.05 C (1 C = 270 mA/g, calculated by assuming full extraction/insertion of Mg). Electrochemical data was collected using VMP3 potentiostat/galvanostat (Bio-Logic Science Instruments).

Sample characterization

Prior to the characterization of charged and discharged state of $MgMn_2O_4$, electrodes were rinsed thoroughly with triglyme to eliminate the $CsTFSA/Mg(TFSA)_2$ electrolyte and then washed briefly with tetrahydrofuran to remove triglyme. The elemental analysis confirmed that the remaining electrolyte after washing was less than 1 wt% of active mass. The Mg/Mn ratio of the electrodes was chemically analyzed by inductively coupled plasma optical emission spectrometry (ICP-OES).

Calcined powders were characterized by the X-ray powder diffraction (XRPD) analysis on a Rigaku SmartLab diffractometer in the Bragg–Brentano geometry with Cu Kα radiation (λ = 1.5406 Å). XRPD analysis was also performed for charged/discharged samples sealed in a Lindeman glass capillary using the beamline BL02B2 of SPring-8 in the Debye-Scherrer geometry with synchrotron radiation (λ = 0.7000 Å) or using Rigaku SmartLab diffractometer in the Debye-Scherrer geometry with Mo Kα radiation (λ = 0.7926 Å). Experimental diffraction patterns were compared with simulated patterns produced with VESTA program[24].

The XPS measurements were carried out in RIKEN using a VG ESCALAB 250 spectrometer (Thermo Fisher Scientific K.K.) employing monochromatic Al Kα X-ray radiation. The system was operated at 15 kV and 200W. The base pressure of the analysis chamber was less than 10^{-8} Pa. These characterizations were carried our using transfer vessel to avoid moisture /air exposure of the samples. Binding energy was calibrated with F 1s spectra (687.8 eV) of PVDF.

Energy dispersive X-ray spectroscopy (EDX) was carried out on a JEOL JEM-ARM200F scanning transmission electron microscope (STEM) operated at 200 kV. Elemental mapping data were analyzed with JEOL Analysis Station software. Atomic-resolution STEM images were obtained with a spherical-aberration-corrected FEI Titan^3 G2 60-300 S/TEM operated at 300 kV. High frequency noise was removed through low-pass filtering with Digital Micrograph software.

Results and discussion

The spinel $MgMn_2O_4$ powder was synthesized through Pechini's method followed by calcination at 425°C. Fig. 1 shows the X-ray diffraction pattern obtained for the calcined powder, along with diffraction patterns simulated for tetragonal spinel structures. Here we adopt crystallographic notation (lattice constant, orientation, etc.) for tetragonal spinels based on an unconventional F-centered tetragonal lattice (Fig. S2) to make it

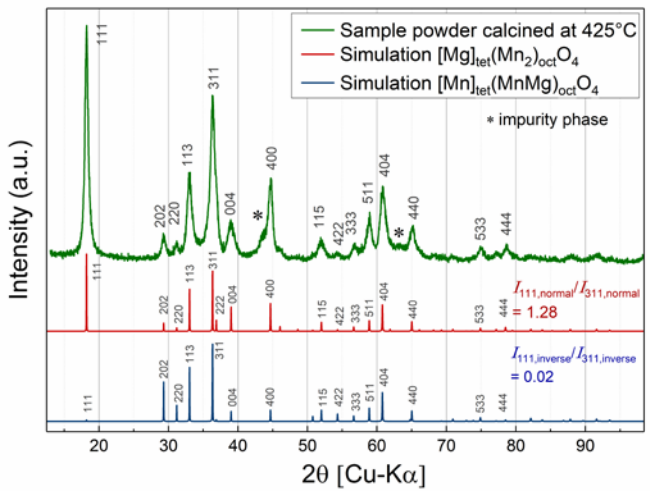

Fig. 1. The XRD pattern of $MgMn_2O_4$ calcined at 425 °C. The simulations are based on tetragonal spinel structure ($I4_1/amd$). The asterisk (*) denotes impurity phase. Indices of the tetragonal spinel are converted to the same orientation as the cubic spinel by adopting a *F*-centered tetragonal lattice.

easy to compare a tetragonal spinel ($I4_1/amd$) and a cubic spinel (Fd-3m). Although small peaks at 44° and 63° implied the existence of some impurity phase (indicated by * in the profile), the overall diffraction pattern was substantially indexed based on a tetragonal spinel structure ($I4_1/amd$). As shown in the two simulations, the relative intensity of 111 diffraction peak reflects the degree of inversion between the tetrahedral sites and the octahedral sites. Depending on the inversion degree, the peak-intensity ratio, I_{111}/I_{311}, ranges from 1.28 (for normal spinel) to 0.02 (for inverse spinel) without taking account of Debye-Waller factor B as a temperature effect, whereas the value of I_{111}/I_{311} is larger when considering the temperature effect; for example, I_{111}/I_{311} ~ 1.4 when B = 1.5. Actually, the I_{111}/I_{311} value of the sample was estimated to be about 1.4, which strongly indicates that the present $MgMn_2O_4$ is of normal type configuration and Mn predominantly occupies octahedral sites while Mg does tetrahedral sites. Malavasi *et al*.[25] reported that $MgMn_2O_4$ synthesized through solid-state reaction at 1200 °C has a degree of inversion over 20%. The $MgMn_2O_4$ powder synthesized in this study tends to show a higher degree of order (i.e., normal-like) due to the calcination temperature as low as 425 °C. The origin of tetragonal symmetry in which c/a ratio is larger than unity can be explained by Jahn-Teller distortion of Mn(III) at octahedral sites[26]. TEM observation of the calcined powder showed that the size of primary particles is 50–100 nm (Fig. S3).

The electrochemical behavior of $MgMn_2O_4$ was evaluated at 150 °C using an ionic liquid electrolyte composed of 90 mol% CsTFSA and 10 mol% $Mg(TFSA)_2$, which possess a high thermal stability up to about 200–300 °C [27]. Prior to a detailed examination of Mg deintercalation, the redox activity of $MgMn_2O_4$ was investigated by the cyclic voltammetry in a wide potential range (Fig. 2a). Within the potential range of 2.0–4.5 V vs. LiRE, $MgMn_2O_4$ exhibits two redox pairs of anodic and cathodic peaks. Based on our previous report[16], the redox pair around 2.9 V vs. LiRE corresponds to two-phase reaction

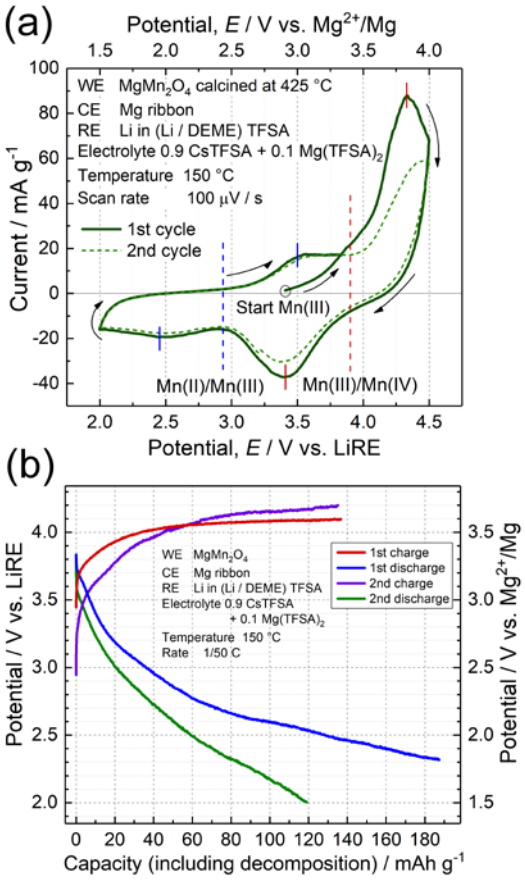

Fig. 2. (a) Cyclic voltammogram of $MgMn_2O_4$ electrode. The electrode potential of Mg^{2+}/Mg is also shown referring to the previous report[16] associated with the reference-electrode conversion. (b) Charge/discharge cycles at 1/50 C.

between spinel $MgMn_2O_4$ and rocksalt $Mg_{1+x}Mn_2O_4$; also the present study confirmed the formation of a rocksalt phase using XRD analysis (Fig. S4). In contrast, the redox pair around 3.9 V vs. LiRE is ascribed to Mg deintercalation from the spinel and subsequent Mg intercalation into the spinel host. This redox pair at higher potential was also observed in the second cycle, suggesting the reversibility of the Mg deintercalation/intercalation reaction.

The redox behavior was also investigated at a constant-current condition (1/50C); see Fig. 2b. Up to the amount of 100 mAh/g during the first charge, Mg is considered to be extracted from the host, resultingly, to form $Mg_{1-x}Mn_2O_4$, while the potential plateau around 100–140 mAh/g suggests that the electrolyte would be oxidized instead of Mg extraction from $MgMn_2O_4$. Nevertheless, the subsequent discharge started from a higher potential than OCP (3.4 V vs. LiRE), indicating that Mg was extracted from $MgMn_2O_4$ during the first charge. The capacity of the first discharge (187 mAh/g) larger than that of charge arises not only from $xMg^{2+} + 2xe^- + Mg_{1-x}Mn_2O_4 \rightarrow MgMn_2O_4$ (i.e., the reduction from Mn(IV) to Mn(III)) but also from $Mg^{2+} + 2e^- + MgMn_2O_4 \rightarrow Mg_2Mn_2O_4$ (i.e., the reduction from Mn(III) to Mn(II)). From the cyclic voltammogram in Fig.2a, it can be inferred that the rocksalt phase (consisting of Mn(II)) is also formed below 2.9 V vs LiRE in the discharge profile; actually the

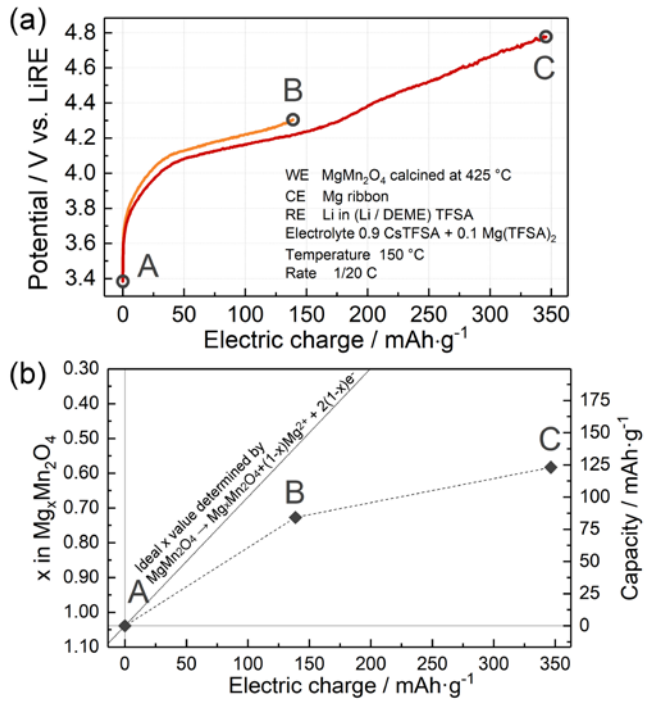

Fig. 3. (a) Galvanostatic charge profile of $MgMn_2O_4$ at a rate of C/20. Pristine $MgMn_2O_4$ denoted by A was charged up to B (along an orange curve) and C (along a red curve). Electric charge shown in the bottom axis includes charge transfer due to side-reactions as well as Mg-deintercalation. (b) Composition of the electrodes A, B and C corresponding to Fig. 3a. The composition was measured by ICP-OES. Electric charge shown in the bottom axis also corresponds to Fig. 3a. A broken line shows ideal Mg content when assuming that Mg-deintercalation occurs without electrolyte decomposition.

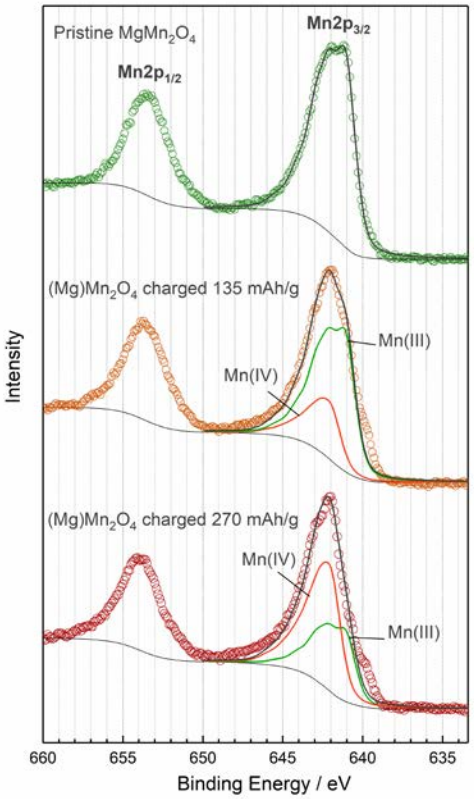

Fig. 4. Mn 2p XPS spectra of pristine and charged $MgMn_2O_4$, which is denoted as $(Mg)Mn_2O_4$. The electrodes were galvanostatically charged at a rate of C/20 at 150 °C. Note that the electric charge of 135 and 270 mAh/g involves electrolyte decomposition as well as Mg-deintercalation. Peak deconvolution was performed using the spectrum of pristine $MgMn_2O_4$ as Mn(III) component and that of MnO_2[29] as Mn(IV) component.

second charge process started from about 2.9 V, which indicates the rocksalt formation near the particle surface (this will be discussed later in Fig. 8).

In order to obtain a compositional evidence of Mg deintercalation, Mg content was analyzed by ICP-OES after various amounts of galvanostatic charge. Fig. 3a shows initial charge curves for $MgMn_2O_4$ at a rate of C/20 to different amounts of electric charges. $MgMn_2O_4$ electrodes of (A) pristine state were galvanostatically oxidized to different electric charges, corresponding to the capacities of (B) 139 mAh/g and (C) 347 mAh/g. Here, note that (C) was oxidized beyond theoretical capacity of 270 mAh/g, because the measured electric charges partially involved electrolyte decomposition. Fig. 3b shows the atomic ratio of Mg and Mn analyzed by ICP-OES. Assuming a chemical formula of $Mg_xMn_2O_4$, the values of x in (A), (B) and (C) were determined to be 1.04, 0.73 and 0.58, respectively. This remarkable decrease in Mg content upon oxidation suggests that Mg ions can be electrochemically deintercalated from spinel $MgMn_2O_4$. The decrease of 0.46 (= 1.04 - 0.58) in the Mg content actually amounts to 124 mAh/g in capacity. The broken line shows ideal Mg content determined by assuming that Mg deintercalation takes place without electrolyte decomposition. The growing difference between ideal and actual Mg content with increase in electric charge represents the difficulty in extracting all the Mg ions from $MgMn_2O_4$. In particular, steep increase in operating potential in the latter half of charge indicates the existence of kinetic limitations to full Mg deintercalation, which would be related to the loss of concerted interaction that facilitates the ionic motions in the cathode host when it contains a certain amount of cations.[28]

The valence state of Mn after Mg extraction was investigated by XPS. Fig. 4 shows Mn XPS spectra of $MgMn_2O_4$ with different charged state. Pristine $MgMn_2O_4$ showed a broad Mn $2p_{3/2}$ spectrum similar to Mn_2O_3 and MnOOH[29] in terms of peak shape and binding energy, which confirms the presence of Mn(III) within $MgMn_2O_4$. Upon charging, the Mn $2p_{3/2}$ spectra shifted to higher binding-energy side, indicating the oxidation of Mn(III) to Mn(IV); see the overlapped spectra in Fig. S5 for comparison. The reason why the Mn 2p spectra coming from Mn compounds are generally broad and asymmetric is described in detail in Ref. 30. This is also the case for the present Mn 2p spectra. The presence of Mn(IV) after charging 270 mAh/g is also qualitatively confirmed by the peak shape similar to δ-MnO_2[29]and γ-MnO_2[30]. The Mn(III)/Mn(IV) ratio upon charging was estimated by optimizing intensity ratios of Mn(III) and Mn(IV) XPS profiles, where the spectrum of pristine $MgMn_2O_4$ is used for Mn(III), and that of MnO_2[29] is for Mn(IV); both curves of Mn(III)and Mn(IV)were reproduced from the several multiplet splitting peaks (Gaussian–Lorentzian

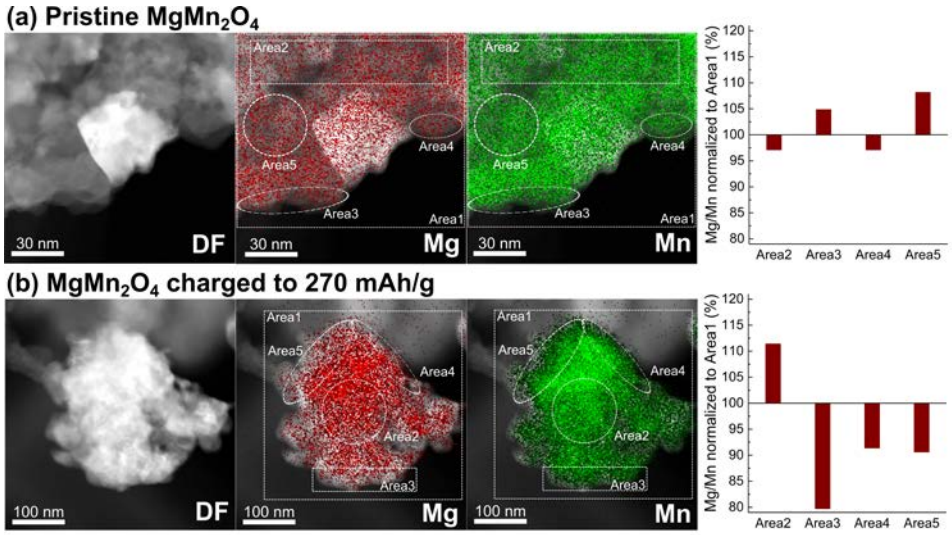

Fig. 5. STEM-EDX mapping of (a) pristine $MgMn_2O_4$ and (b) $MgMn_2O_4$ charged to 270 mAh/g. Left: Dark field images. Middle: Mg maps. Right: Mn maps. Mg/Mn ratios in each area are normalized to that of Area1.

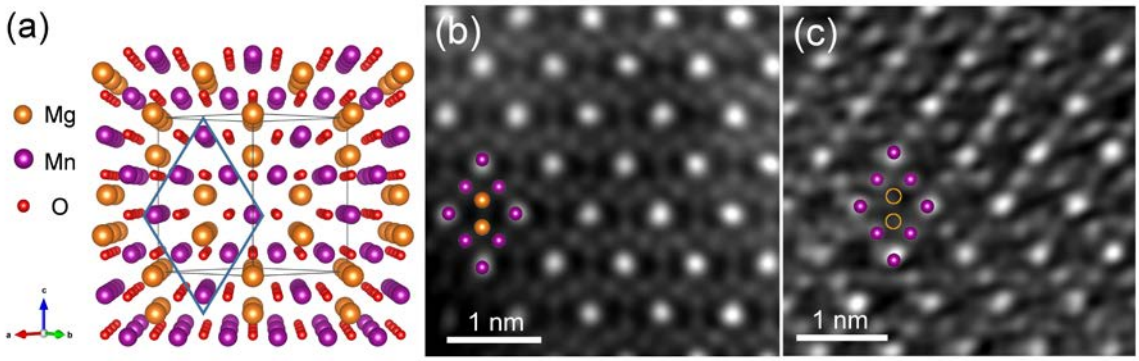

Fig. 6. (a) Perspective view of tetragonal spinel $MgMn_2O_4$ viewed along [110] direction. (b) HAADF-STEM image of pristine $MgMn_2O_4$ viewed along the [110] direction. (c) HAADF-STEM image of $MgMn_2O_4$ charged to 270 mAh/g viewed along the [110] direction. Superimposed atomic illustration shows the position of atomic columns.

functions) with the same fixed FWHM parameter (=1.38) and Gaussian/Lorentzian ratio (=47:53). After charging of 135 mAh/g (nominal value), Mn(III)/Mn(IV) ratio was 74:26 that is equivalent to $Mn^{+3.26}$ in average (i.e., 0.26 Mg extraction), being well comparable with the present ICP result (see, Fig. 3b). After charging of 270 mAh/g (nominal involving electrolyte decomposition), Mn(III)/Mn(IV) ratio was 40:60 that is equivalent to $Mn^{+3.60}$ (i.e., 0.60 Mg extraction). The extraction amount of 0.60 Mg discrepantly exceeds ~ 0.3 Mg estimated from the ICP analysis in Fig. 3b; however, the lower Mg concentration on the surface could be reasonably explained by a two-phase reaction, where a Mg-poor phase would appear near the surface of active materials upon charge.

Local distribution of Mg and Mn after charge was investigated by the STEM-EDX analysis. Fig. 5 shows the EDX mapping of pristine and charged $MgMn_2O_4$. The ratios of Mg/Mn elements in the whole image (Area1) were 0.41 and 0.36 in pristine and charged spinels, respectively. The Mg/Mn ratios obtained from the respective areas (Area2–Area5) in the images are normalized to the Mg/Mn ratio of the whole area (Area1). Regardless of the position in matrix, the pristine $MgMn_2O_4$ exhibits similar Mg/Mn ratios with relatively small variations (within about 10%), confirming the homogeneous distribution of Mg in the pristine sample. In contrast, Mg/Mn ratios in charged $MgMn_2O_4$ exhibits larger variations depending on the positions. Specifically, the Mg concentrations (Area3-Area5) on the particle surface was significantly lower by about 20% than the average concentration (Area1). This concentration variation indicates the occurrence of Mg deintercalation from the sample surface, namely, core-shell structure was attained after charge.

To further confirm the Mg deintercalation, we directly observed the demagnesiated $MgMn_2O_4$ after charge using STEM. According to the XRD profile, tetragonal spinel $MgMn_2O_4$ likely has a highly ordered (normal-type like) cation configuration, as illustrated in Fig. 6a. In the ordered structure, columns of Mg and Mn atoms can be clearly distinguished when viewed along the [110] direction. Fig. 6b,c shows high-angle annular dark-field (HAADF) images of pristine and charged $MgMn_2O_4$ viewed along [110] direction. The pristine spinel exhibits homogeneous Z-contrast both at tetrahedral sites and at octahedral sites, being in good agreement with the ordered structure of tetragonal spinel $MgMn_2O_4$. The charged spinel shows significantly weak and heterogeneous contrast at the Mg columns, indicating that Mg vacancies are formed by charging.

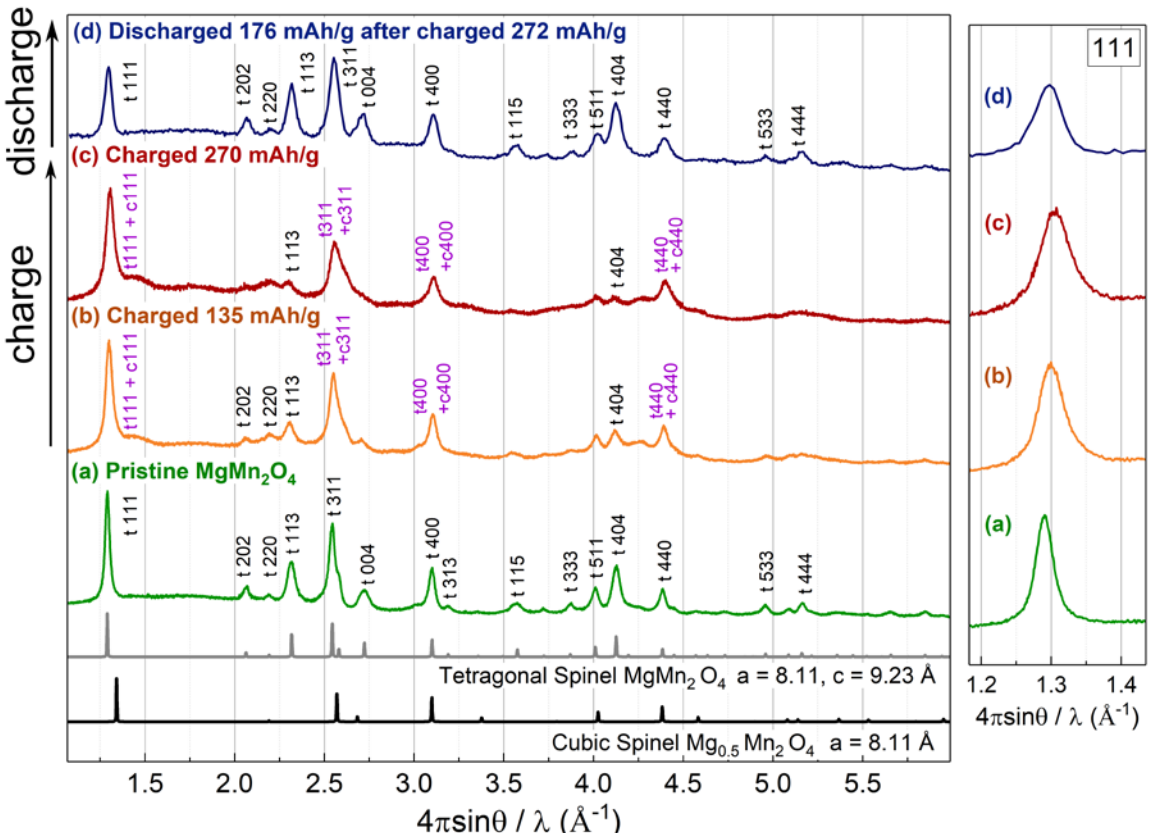

Fig. 7. XRD patterns of $MgMn_2O_4$ electrodes with different charged and discharged state. (a) pristine $MgMn_2O_4$ electrode. (b) $MgMn_2O_4$ galvanostatically charged to 135 mAh/g. (c) $MgMn_2O_4$ galvanostatically charged to 270 mAh/g. (d) $MgMn_2O_4$ charged to 272 mAh/g and subsequently discharged to 176 mAh/g using GITT to mitigate electrolyte decomposition. Gray line shows a calculated diffraction pattern of normal spinel $MgMn_2O_4$ with tetragonal symmetry ($I4_1/amd$) while black line shows calculated diffraction pattern of normal spinel $Mg_{0.5}Mn_2O_4$ with cubic symmetry (Fd-3m). Diffraction peaks assigned to the tetragonal and cubic spinels are marked with t and c, respectively. Indices of the tetragonal spinel are converted to the same orientation as the cubic spinel by defining a F-centered tetragonal lattice.

On the other hand, contrast at the Mn columns remains almost unchanged after charge, which shows that the demagnesiated spinel host maintains the framework, even though the spinel is charged at 150 °C. The inhomogeneous contrast at the tetrahedral sites indicates that Mg cations partially remain within the spinel. In addition, Mg-vacancy formation may cause some degrees of inversion between tetrahedral sites and octahedral sites[31]. Therefore, some atoms at tetrahedral sites could be not only Mg, but also Mn. The formation of Mg-poor phase near the surface of particles are in good agreement with the XPS/ICP results.

Structural change of $MgMn_2O_4$ after charge and discharge was investigated with ex-situ X-ray powder diffraction experiments, the results of which are shown in Fig. 7. First of all, note that the splitting peaks of 113/311, 004/400 and 404/440 reflect the c/a ratio exceeding unity. As a significant change before/after charge, the 113, 004 and 404 diffraction peaks gradually disappear as $MgMn_2O_4$ is charged from (a) a pristine state to (c) a charged state up to 270 mAh/g (involving electrolyte decomposition, and corresponding to extraction of 0.3-0.4 Mg from $MgMn_2O_4$ with reference to Fig. 2). When a tetragonal spinel transforms into a cubic spinel, it is naturally expected that the splitting peaks converge into one diffraction peak. Thus, the decreases in the intensity ratios 113/311, 004/400 and 404/440 strongly suggest that the original tetragonal spinel transforms into a cubic spinel by Mg-deintercalation. In addition, the structure factors of the 202 and 220 peaks are function only of the atomic scattering factor located at 8a site in the spinel structure (Fig. S6). The intensity decreases in these peaks indicate the Mg extraction from the normal spinel structure as well. Nevertheless, it deserves to note that the cubic-like spinel seemingly has a tetragonality (c/a >1) to some degree; this would be due to a constrained strain when the cubic spinel is coherently formed in the tetragonal matrix, as can be inferred from broadening diffraction peaks after charge. The characteristic peaks of the tetragonal spinel (113, 004 and 404) hardly shift while charging; consequently, we conclude that Mg-deintercalation from $MgMn_2O_4$ proceeds through a two-phase reaction between the tetragonal spinel and a cubic spinel. This conclusion is also supported by XRD simulations comparing two-phase behavior and single-phase behavior; see Fig. S7-S8. The disappearance of the tetragonal anisotropy is attributed to the oxidation of Mn(III) that induces Jahn-Teller distortion. Finally, Fig. 7 (d) demonstrates that subsequent discharge from a charged state (about 270 mAh/g) virtually reverts to a tetragonal spinel phase. However, note that the relative intensity of 111/311 peaks decreased compared to that for the pristine spinel. As shown in a XRD simulation in Fig. S9, decrease of 111 diffraction peak can be caused by inversion between Mg at tetrahedral site and Mn at octahedral site. Recently,

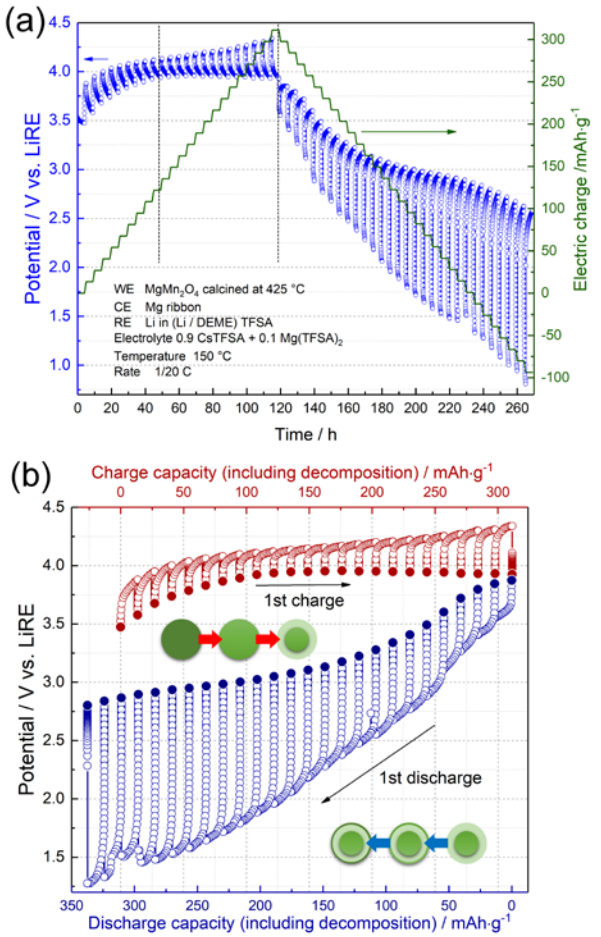

Fig. 8. The charge/discharge profile of $MgMn_2O_4$ obtained using GITT. (a) The evolution of the electrode potential as a function of elapsed time during the GITT measurement. Electrode potential (blue circles) corresponds to the left axis while capacity (green line) corresponds to the right axis. (b) The electrode potential as a function of the capacity. The capacity includes electrolyte decomposition as well as the redox reaction of $MgMn_2O_4$.

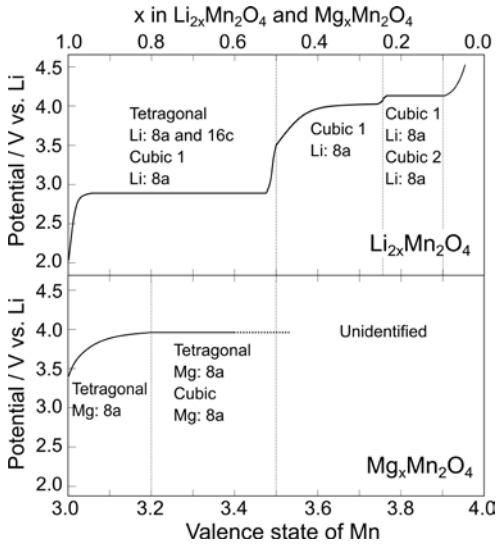

Fig. 9. Schematic diagram to compare the phase transition of spinel $LiMn_2O_4$ and spinel $MgMn_2O_4$. Potential profile of $LiMn_2O_4$ is schematically illustrated based on refs. 32-35. Potential profile of $MgMn_2O_4$ is based on equilibrium potential shown in Fig. 8.

theoretical calculation by Gautam *et al.*[31] revealed that non-inverted spinel $(Mg_x\square_{1-x})_{tetrahedral}[Mn_2]_{octahedral}O_4$ could be thermodynamically unstable at intermediate Mg composition, where □ denotes the vacancy in the tetrahedral site. Our experiment also suggests that originally normal $MgMn_2O_4$ undergoes inversion after Mg-extraction/insertion cycle.

To clarify the more detailed features in the two-phase reaction of the tetragonal and cubic spinel, we performed charge and discharge tests using GITT to obtain equilibrium potential of $MgMn_2O_4$ (Fig. 8a). As we mentioned in Fig. 2b, Mg deintercalation from $MgMn_2O_4$ is accompanied by some side reactions (e.g., oxidative decomposition of the electrolyte) at higher potentials, but to see the conventional battery test tetragonal spinel undergoes a single-phase reaction at the beginning of deintercalation. While charging up to about 320 mAh/g (c.a. 0.4 Mg extraction referring to Fig. 2b) beyond 120 mAh/g, the equilibrium potential obviously remains constant at 3.9 V vs. LiRE; thus, we confirmed that until Mg content is about x = 0.6, the two-phase equilibrium holds. In the subsequent discharge process, the capacity amounted to 70-80 mAh/g until the potential reverted back to the initial OCP value of $MgMn_2O_4$ (3.4 V), which indicates that about 0.26-0.30 Mg is reversibly intercalated into $MgMn_2O_4$ (given that there is no cathodic side reaction in the discharge process). This could extend the feasible capacity of $MgMn_2O_4$ (spinel $MgMn_2O_4 + Mg^{2+} + 2e^- =$ rocksalt $Mg_2Mn_2O_4$: 270 mAh/g)[16] that occurs below the initial OCP of $MgMn_2O_4$ (see Fig. S4). However, the Mg intercalation unfortunately requires large overpotentials, consequently causing the decomposition of $TFSA^-$ anion (below 1.5 V vs LiRE). Similarly, it should be noted that the single-phase reaction tends to take place in the discharge process without showing any plateau (i.e. two-phase reaction), and this can be understood also in terms of kinetics; inserted Mg tends to be accumulated around the surface of active materials (as seen in the inset in Fig. 8b) due to the sluggish diffusion of Mg in the spinel.

Finally, let us discuss about the difference in the transformation mode between spinel $MgMn_2O_4$ and spinel $LiMn_2O_4$. Such a comparison of the structural changes of the two spinel compounds will provide a clue to consider the difference between divalent and monovalent intercalation chemistry. Fig. 9 schematically illustrates the potential profile of $LiMn_2O_4$ and $MgMn_2O_4$ as a function of the Mn valence between 3.0 and 4.0. Li intercalation process involves three phases: tetragonal $Li_2Mn_2O_4$, cubic spinel $Li_{2x}Mn_2O_4$ (0.5 > x > 0.25) and cubic λ-$Li_{2x}Mn_2O_4$ (0.1 > x > 0.0). Whereas, Mg intercalation process involves tetragonal spinel $Mg_xMn_2O_4$ and cubic spinel $Mg_xMn_2O_4$. Based on the present results, we estimate that a two-phase region of tetragonal/cubic Mg spinels appears below x = 0.8. Both Li and Mg spinels exhibit tetragonal phases between 3.0 and 3.5 in the Mn valence due to the Jahn-Teller effect; namely, the Mn valence is a dominant factor in determining crystal systems. The tetragonal $Mg_xMn_2O_4$ (1.0 > x > 0.8) exhibits an electrode potential similar to that of cubic $Li_{2x}Mn_2O_4$ (0.5 > x > 0.25), which means that one-Mg insertion into 8*a* sites produces free energy change comparable to two-Li insertion. Furthermore, the electrode potential of tetragonal

$Mg_xMn_2O_4$ (x = 1) is higher than that of tetragonal $Li_{2x}Mn_2O_4$ (x = 1). This is presumably because divalent Mg ion located at 8a site can lower the Madelung energy more effectively than monovalent Li ion pair that causes a repulsive interaction between the cations. Incidentally, the inserted Li pair is considered to be located around 8a site or at two respective 16c sites; but it is still unclear which is realized after the Li insertion, holding the spinel structure (the former) or transforming to a rocksalt-like structure (the latter).

Conclusions

In summary, this work highlighted the inherent potential of spinel oxide cathodes for magnesium rechargeable batteries (MRBs) with high energy density. Especially focusing on $MgMn_2O_4$ normal spinel, we have demonstrated the feasibility of electrochemical deintercalation/intercalation of Mg from/into the spinel cathode in non-aqueous electrolyte at a moderate temperature.

$MgMn_2O_4$ powder synthesized through the Pechini method forms a spinel structure with tetragonal symmetry due to Jahn-Teller distortion of trivalent Mn(III). It has been shown that electrochemical oxidation in an ionic liquid electrolyte at 150 °C allows Mg-deintercalation from $Mg_xMn_2O_4$. The minimum Mg composition achieved in the present study was x = 0.6. From x = 1.0 to x = *ca*. 0.8, the deintercalation of Mg from $Mg_xMn_2O_4$ occurs via single-phase reaction with keeping the tetragonal spinel. Below ca. x = 0.8, the Mg deintercalation from $Mg_xMn_2O_4$ proceeds via two-phase reaction of the tetragonal spinel and a Mg-defect (demagnesiated) cubic spinel. The Mg intercalation into the defect cubic spinel also allows reversible phase transformation into the original tetragonal spinel.

The λ-Mn_2O_4 framework in $MgMn_2O_4$ is substantially identical to that in $Li_2Mn_2O_4$ in terms of the valence state of Mn and Jahn-Teller distortion. As seen in Fig. 9, despite the identical valence state of Mn, Mg^{2+} insertion into λ-Mn_2O_4 exhibits a higher electrode potential than a pair of Li^+ insertion into λ-Mn_2O_4. This potential difference implies that Mg^{2+} cation more effectively lowers the Madelung energy compared to a pair of Li^+ ions possessing a repulsive interaction of intrapair.

A cathode performance of $MgMn_2O_4$ may be improved by partial substitution of Mn with another transition metal to prevent (1) Jahn-Teller distortion and (2) a two-phase reaction. Due to Jahn-Teller distortion, $MgMn_2O_4$ undergoes a large anisotropic volume change during the Mn(III)/Mn(IV) redox reaction. Therefore, the suppression of the Jahn-Teller distortion would be an important strategy to alleviate the strain in the active material and unfavorable morphological change. The two-phase system would be the origin of large polarization/overpotential during a discharge process, because sluggish Mg diffusion and coherent strain consequently lead to the formation of a core-shell morphology, where the particle surface is fully occupied by Mg ions. Doping effective elements to induce a single-phase reaction, therefore, is considered to improve the Mg insertion kinetics in $MgMn_2O_4$-based active materials.

In this work, in order to clearly investigate Mg-extraction/insertion behavior from the scientific viewpoint, Mg diffusion kinetics were enhanced by elevating a cell temperature up to 150 °C. On the other hand, increasing the operation temperature would become disadvantageous in terms of stable cycling and practical application. Therefore, practical use of $MgMn_2O_4$ would require other methods to improve Mg diffusion kinetics such as co-insertion of Li ions[28].

Conflicts of interest

There are no conflicts to declare.

Acknowledgements

The authors acknowledge funding support from the Advanced Low Carbon Technology Research and Development Program (ALCA, Grant number: JPMJAL1301). We are also grateful to Professor K. Kanamura for valuable comments and direction to this study.

Notes and references

1 M. Armand and J.-M. Tarascon, *Nature*, 2008, **451**, 652–657.
2 J.-M. Tarascon and M. Armand, *Nature*, 2001, **414**, 359–367.
3 M. M. Thackeray, C. Wolverton and E.D. Isaacs, *Energy. Environ. Sci.*, 2012, **5**, 7854–7863.
4 B. Dunn, H. Kamath and J.-M. Tarascon, *Science,* 2011, **334**, 928–935.
5 Z. Yang, J. Zhang, M.C.W. Kintner-Meyer, X. Lu, D. Choi, J.P. Lemmon and J. Liu, *Chem. Rev.*, 2011, **111**, 3577–3613.
6 E. Levi, Y. Gofer and D. Aurbach, *Chem. Mater.*, 2010, **22**, 860–868.
7 P. Canepa, G. Sai Gautam, D.C. Hannah, R. Malik, M. Liu, K.G. Gallagher, K. A. Persson and G. Ceder, *Chem. Rev.*, 2017, **117**, 4287–4341.
8 D. Aurbach, Z. Lu, A. Schechter, Y. Gofer, H. Gizbar, R. Turgeman, Y. Cohen, M. Moshkovich and E. Levi, *Nature*, 2000, **407**, 724–727.
9 Y. Orikasa, T. Masese, Y. Koyama, T. Mori, M. Hattori, K. Yamamoto, T. Okado, Z.-D. Huang, T. Minato, C. Tassel, J. Kim, Y. Kobayashi, T. Abe, H. Kageyama and Y. Uchimoto, *Sci. Rep.*, 2014, **4**, 5622.
10 G. Gershinsky, H. D. Yoo, Y. Gofer and D. Aurbach, *Langmuir*, 2013, **29**, 10964–10972.
11 R. Zhang, X. Yu, K.-W. Nam, C. Ling, T. S. Arthur, W. Song, A. M. Knapp, S. N. Ehrlich, X.-Q. Yang and M. Matsui, *Electrochem. Commun.*, 2012, **23**, 110–113.
12 K. W. Nam, K. W. Nam, S. Kim, S. Lee, M. Salama, I. Shterenberg, Y. Gofer, J.-S. Kim, E. Yang, C. S. Park, J.-S. Kim, S.-S. Lee, W.-S. Chang, S.-G. Doo, Y. N. Jo, Y. Jung, D. Aurbach and J. W. Choi, *Nano Lett.*, 2015, **15**, 4071–4079.
13 X. Sun, V. Duffort, B. L. Mehdi, N. D. Browning and L. F. Nazar, *Chem. Mater.*, 2016, **28**, 534–542.
14 J. Song, M. Noked, E. Gillette, J. Duay, G. Rubloff and S. B. Lee, *Phys. Chem. Chem. Phys.*, 2015, **17**, 5256–5264.
15 T. Ichitsubo, T. Adachi, S. Yagi and T. Doi, *J. Mater. Chem.*, 2011, **21**, 11764.
16 S. Okamoto, T. Ichitsubo, T. Kawaguchi, Y. Kumagai, F. Oba, S. Yagi, K. Shimokawa, N. Goto, T. Doi and E. Matsubara, *Adv. Sci.*, 2015, **2**, 1500072.

17 M. M. Thackeray, W. I. F. David, P. G. Bruce and J. B. Goodenough, *Mater. Res. Bull.*, 1983, **18**, 461–472.
18 M. M. Thackeray, P. J. Johnson, L. A. de Picciotto, P. G. Bruce and J. B. Goodenough, *Mater. Res. Bull.*, 1984, **19**, 179–187.
19 J. M. Tarascon, E. Wang, F. K. Shokoohi, W. R. McKinnon and S. Colson, *J. Electrochem. Soc.*, 1991, **138**, 2859–2864.
20 C. Kim, P. J. Phillips, B. Key, T. Yi, D. Nordlund, Y. S. Yu, R. D. Bayliss, S.-D. Han, M. He, Z. Zhang, A. K. Burrell, R. F. Klie and J. Cabana, *Adv. Mater.*, 2015, **27**, 3377–3384.
21 N. L. Okamoto, K. Shimokawa, H. Tanimura, T. Ichitsubo, , *Scr. Mater.*, 2019, **167**, 26–30
22 K. Shimokawa, T. Atsumi, M. Harada, R.E. Ward, M. Nakayama, Y. Kumagai, F. Oba, N. L. Okamoto, K. Kanamura, T. Ichitsubo, *J. Mater. Chem. A*, 2019, **7**, 12225–12235.
23 T. Ohzuku, M. Kitagawa and T. Hirai, *J. Electrochem. Soc.*, 1990, **137**, 769–775.
24 K. Momma and F. Izumi, *J. Appl. Crystallogr.*, 2011, **44**, 1272–1276.
25 L. Malavasi, P. Ghigna, G. Chiodelli, G. Maggi, G. Flor, *J. Solid State Chem.* 2002, **166**, 171-176.
26 A. Yamada, M. Tanaka, K. Tanaka and K. Sekai, *J. Power Sources* 1991, **81-82**, 73–78.
27 R. Hagiwara, K. Tamaki, K. Kubota, T. Goto and T. Nohira, *J. Chem. Eng. Data*, 2008, **53**, 355–358.
28 H. Li, N. L. Okamoto, T. Hatakeyama, Y. Kumagai, F. Oba and T. Ichitsubo, *Adv. Energy Mater.*, 2018, **8**, 1801475.
29 M. C. Biesinger, B. P. Payne, A. P. Grosvenor, L. W. M. Lau, A. R. Gerson and R. S. C. Smart, *Appl. Surf. Sci.*, 2011, **257**, 2717–2730.
30 M. Minakshi Sundaram, A. Biswal, D. Mitchell, R. Jones and C. Fernandeze, *Phys. Chem. Chem. Phys.*, 2016, **18**, 4711–4720.
31 G. Sai Gautam, P. Canepa, A. Urban, S.-H. Bo and G. Ceder, *Chem. Mater.*, 2017, **29**, 7918-7930.
32 T. Ohzuku, M. Kitagawa and T. Hirai, *J. Electrochem. Soc.*, 1990, **137**, 40–46.
33 M. M. Thackeray, *Prog. Solid State Chem.*, 1997, **25**, 1–71.
34 W. I. F. David, M. M. Thackeray, L. A. De Picciotto and J. B. Goodenough, *J. Solid State Chem.*, 1987, **67**, 316–323.
35 M. M. Thackeray, W. I. F. David, P. G. Bruce and J. B. Goodenough, *Mater. Res. Bull.* 1983, **18**, 461–472.